Ordered mesoporous Au/TiO$_2$ nanospheres for solvent-free visible-light-driven plasmonic oxidative coupling reactions of amines

Jingling Yang, Chung-Yuan Mou*

Department of Chemistry, National Taiwan University, Taipei 10617, Taiwan

ABSTRACT

Imines are important intermediates for the synthesis of fine chemicals and pharmaceuticals. Design of a "green" oxidation catalyst to promote the direct oxidation of amines to imines by dioxygen have attracted great attention. Herein, we designed a catalyst of ordered mesoporous Au/M-TiO$_2$ nanoparticles using a template-based approach. The as-prepared Au/M-TiO$_2$ nanoarrays of anatase crystalline structure, with high specific surface area (222 m^2/g), small pore size (~2.1 nm) and ordered arrangements, gave dense array of ultrasmall pore-confined gold nanoparticles. The mesoporous Au/M-TiO$_2$ exhibits particularly high visible light activity for photocatalytic selective aerobic oxidation of benzylamine to *N*-benzylidene benzylamine in a green approach by utilizing dioxygen as an oxidant in solvent-free conditions. The yield of *N*-benzylidene benzylamine can reach 1.73 mmol (TOF = 178.6 h^{-1}, based on Au) in Au/M-TiO$_2$ system, which is 1.5 and 1.6 times higher than that of the Au/P25 and Au/Acros anatase photocatalysts, respectively. Furthermore, we can also achieve high yield of *N*-benzylidene benzylamine (1.30 mmol, TOF = 134.2 h^{-1}, based on Au) in air atmosphere. The confinement effect of the mesopores in Au/M-TiO$_2$ facilitate the formation of ·O$_2^-$ radicals and make the bi-molecular reaction highly preferred for promoting the high selectivity and conversion in plasmonic photocatalysis. Meanwhile, the Au/M-TiO$_2$ with mesoporous structure can facilitate the efficient contact between the solvent and the nanomaterial, while possessing sufficient interfacial area for active oxidation reactions. This work paves a promising way to develop visible light-responsive TiO$_2$-based photocatalysts with high specific surface area for highly efficient green oxidative organic synthesis.

1. Introduction

Catalytic oxidation of amine to imine is of intense interest since imines are important versatile intermediates for fine chemicals and pharmaceuticals [1–4]. In industrial production, imines are synthesized by the condensation of amines with aldehydes in organic solvents at elevated temperatures [5]. However, the highly reactive nature of aldehydes make controlling the reaction difficult [6]. Most of the reported methods involve the use of environmentally harmful solvent resulting in pollutants [7,8]. Energy consumption and environmental pollution issues motivate the development of "green" catalytic processes to oxidize amines efficiently and selectively under mild solvent-free condition [9,10]. In recent years, photocatalysis has received significant attention as a green approach for organic synthesis which can efficiently convert solar energy into chemical energy with oxygen as oxidant [11,12]. The development of visible light-induced photocatalysts for transformation of benzylamine into its corresponding imine appears to be a desirable green method. Nevertheless, most of the reported works on the photocatalysis oxidation of amines to imines are conducted in organic solvents, especially in actonitrile, while little attention has been devoted to the reaction in nontoxic solvent or in the absense of solvent [1,2,13]. Recently, Zhu et al. reported water as a viable solvent for the photocatalysis oxidation of benzylamine into *N*-benzylidene benzylamine, but the yield and selectivity were low reaching only 0.16 mmol [6]. Therefore, the development of a green catalytic system for effective conversion of amines into its corresponding imines in solvent free and mild conditions is highly desirable which remains a significant challenge [14,15].

For the reaction, we chose mesoporous titanium dioxide (TiO$_2$) as the catalyst which has become the most extensively studied semiconductor in photocatalytic applications [16]. However, TiO$_2$ possesses a wide band gap (3.2 eV for anatase and 3.0 eV for rutile) which limits its photo-absorption to the UV region, accounting for only ~ 4% of the total sunlight [17,18]. Accordingly, the plasmonic metal (Au, Ag, Cu) nanoparticles (NPs) loaded on wide-band gap semiconductors such as TiO$_2$, have attracted much interest as a new type of photocatalyst in the

visible light range, the so-called "plasmonic photocatalysts" [19,20]. In this process, the plasmonic metals could generate hot electrons by visible light excitation, which are transferred from the excited metal NPs to the semiconductor supports, leaving behind vacant holes [21]. The reductive electrons captured by the supports can convert the adsorbed O_2 molecules into reactive oxygen species, that can participate in catalytic reactions [20]. Since the oxidation catalysis reaction mainly takes place on the surface of the semiconductor support, a high specific surface area is desirable. The low specific surface area of most TiO_2 ($< 100\,m^2/g$) obviously limits the efficiency of plasmonic photocatalysis due to the insufficient reaction sites [22,23]. To overcome this issue, we developed a strategy for synthesizing an ordered mesoporous $Au/M-TiO_2$ plasmonic photocatalyst with high surface area ($222\,m^2/g$) using a template-based method. The $Au/M-TiO_2$ exhibits particularly high visible light activity for selective aerobic oxidation of amines to imines, using a green chemistry approach with dioxygen as the benign oxidant in solvent-free conditions. Furthermore, we can also achieve high yield and selectivity of imine in air atmosphere. This work demonstrates high yield and selectivity of aerobic oxidation of amines to imines and opens the possibility to develop mesoporous Au/TiO_2 for efficient and green organic synthesis.

2. Experimental

2.1. Synthesis

2.1.1. Synthesis of mesoporous silica nanoparticles (MSN)

The synthesis of MSN was reported in our previous work [24,25]. Typically, the cetyltrimethyl ammonium bromide (CTAB) (0.193 g)/ H_2O deionized water (80 g)/decane (600 μL)/ethanol (6.0 g) emulsion was stirred at 50 °C for 12 h before the introduction of ammonia ($NH_3 \cdot H_2O$) solution (1.5 g, 35 wt.%) and tetraethyl orthosilicate (TEOS)/ethanol solution (1.67 mL, 20% v/v). The mixture was stirred at 50 °C for 1 h followed by an aging process, at 50 °C for 20 h. The as-synthesized samples were filtered with a qualitative filter paper (Advantec) to remove side products formed at the oil-water interfaces. The filtered solution was then hydrothermally treated at 80 °C for 24 h. To remove the residual organic surfactants, the samples were treated with a hydrochloric acid/ethanol (5 mg/mL) solution at 50 °C for 16 h under constant stirring followed by centrifugation and sonication with ethanol five times to recover MSN. In the final step, the MSN were vacuum-dried at ambient temperature [24,25].

2.1.2. Synthesis of mesoporous TiO_2 nanoparticle (M-TiO₂)

300 μL of titanium chloride was dissolved into 20 mL hydrochloric acid (36 *wt.*%) solution under constant stirring. Subsequently, 0.15 g of as-prepared MSN powder was mixed with the titanium chloride solution under constant stirring for 2 h. The suspension was then transferred into a 50 mL crucible and dried at 40 °C until all the liquid was evaporated [26]. The dried powder was placed in a muffle furnace for calcination. The temperature was increased from room temperature up to 300 °C at a rate of 1 °C/min and held at 300 °C for 2 h before being cooled down to room temperature. The as-made TiO_2/silica powder was mixed with sodium hydroxide (0.5 mol/L) solution under stirring for 2–3 min and centrifuged to recover the resulting powder. The powder was washed with distilled water twice and dried at 40 °C. The as-prepared sample was labeled as M-TiO₂ (Fig. 1).

2.1.3. Synthesis of mesoporous $Au/M-TiO_2$ nanoparticles

0.3 g of M-TiO₂ were suspended in 100 mL of 3-aminopropyltrimethoxysilane (APTES)/ethanol (1%, v/v) solution and refluxed at 90 °C for 8 h. Then, the functionalized M-TiO₂ were centrifuged and washed with ethanol five times. 0.15 g of the as-prepared functionalized M-TiO₂ was added into 20 mL of HAuCl₄ aqueous solution ($2.5 \times 10^{-4}\,mol/L$), and stirred at 25 °C for 30 min. Then, with an introduction of 1.2 mL of NaBH₄ solution (0.02 mol/L) and stir for 1 min,

then kept aging in the solution for 1 h. Subsequently, the nanocomposites were rinsed with water and vacuum-dried [24]. The as-prepared sample was labeled as $Au/M-TiO_2$. The Au NPs deposited onto the Acros anatase and Degussa P25 use the same procedure as the deposition of Au NPs onto the M-TiO₂.

2.2. Characterization

X-Ray Diffraction (XRD) patterns were recorded on a Bruker D8 Advance with Cu Kα radiation (40 kV, 40 mA). Scanning electron microscopy (SEM) images were obtained using an electron microscope (Hitachi S-4800) at an accelerating voltage of 5.0 kV. Transmission electron microscopy (TEM), high resolution TEM (HRTEM) images, and element mapping results were taken on an FEI Tecnai G2 F30 electron microscope operating at 300 kV and a JEOL JEM-2100F electron microscope operating at 200 kV. A Hitachi U-3010 spectrophotometer was chosen to obtain ultraviolet–visible (UV − vis) diffuse reflectance spectra of the products using $BaSO_4$ as the reference sample. X-Ray photoelectron spectroscopy (XPS) spectra were measured using an X-ray photoelectron spectrometer (Thermo Scientific, Theta Probe). A Micromeritics instrument (ASAP 2010) was used to examine the nitrogen adsorption and desorption properties of the samples at 77 K. Specific surface areas were calculated via the Brunauer–Emmett–Teller (BET) model, and pore size distribution graphs were obtained from the Non-Local Density Functional Theory (NLDFT) model. The electron spin resonance (ESR) spectra were measured using a Bruker Elexsys E-580 electron spin resonance spectrometer, conducted at room temperature with the addition of 5,5-dimethyl-1-pyrroline *N*-oxide (DMPO, BePharm).

2.3. Evaluation of photocatalytic activity

For studying the photocatalysis performance of samples in solvent-free conditions, 30 mg of catalysts were added into neat amine (3 mL) in a sealed reactor (15 mm in diameter and 30 mm in length). The system was first vacuumed and then purged with pure oxygen (99.999 v/v%) for 5 min. Afterwards, the reaction mixture was stirred at 298 K in the dark for 15 min, followed by light irradiation using a 250 W halogen tungsten lamp (HX-500, Wacom) with a UV cut off filter 20CGA-420 (Newport Corporation). The suspension was kept stirring throughout the reaction. The photocatalysis reaction in solvent were conducted in a typical reaction system consisting of a catalyst (20 mg) and benzylamine (0.2 mmol) in acetonitrile (5 mL), and the photoreactions were carried out using the same procedures as above. Then, the selectivity and yield of the products were quantified by gas chromatography–mass spectrometry (GC–MS, Clarus 600/560D) using the calibration curves prepared by decane as an internal standard and each imine products.

3. Results and discussion

3.1. Characterization of ordered mesoporous $Au/M-TiO_2$ nanoparticles

The synthetic process of mesoporous $Au/M-TiO_2$ is illustrated in Fig. 1. Mesoporous silica nanoparticle (MSN), acting as hard template for TiO_2, was synthesized according to previously reported method [24,25]. TiO_2/silica was then obtained through impregnation method and calcination. Subsequently, mesoporous TiO_2 (M-TiO₂) was obtained through removal of silica. Finally, Au nanoparticles were deposited into the nanopores of M-TiO₂. Details are given in experiment section. X-ray diffraction (XRD) was performed to investigate the crystallographic form of as-synthesized mesoporous M-TiO₂ and mesoporous $Au/M-TiO_2$. As shown in Fig. 2a, the XRD peaks of M-TiO₂ and mesoporous $Au/M-TiO_2$ can be indexed to the tetragonal anatase phase of TiO_2 (JCPDS no. 21-1272) [17]. Loading Au nanoparticles to M-TiO₂ did not cause any obvious changes to the crystallinity of M-TiO₂.

Scanning electron microscopy (SEM) images of the MSN, as-
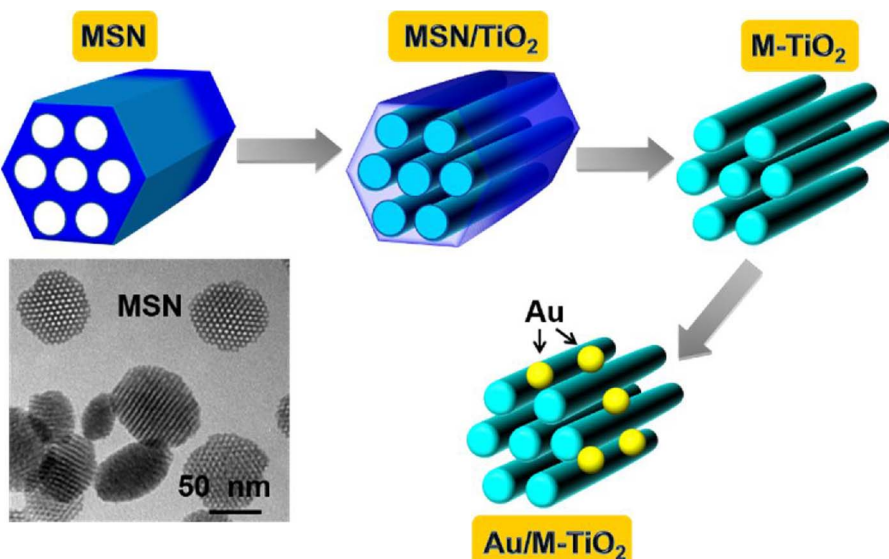
Fig. 1. Synthesis of mesoporous Au/M-TiO$_2$ nanoparticles.

synthesized M-TiO$_2$ and Au/M-TiO$_2$ are shown in Fig. 2b–d, respectively. Fig. 2c shows that M-TiO$_2$ nanoparticles with the replicated spherical shape and size of MSN. After loading Au nanoparticles, the external surface of Au/M-TiO$_2$ became rough and the porous structure of TiO$_2$ are still preserved (Fig. 2c, d), suggesting the presence of Au nanoparticles on the surface. It was difficult to fill titanium precursor into the pore of conventional mesoporous silica with bigger size. The nanospheres of MSN with ordered short channel and pore size of ∼ 4 nm is more suitable hard template for synthesis of mesoporous TiO$_2$. The resulting M-TiO$_2$ thus also possesses the advantages of short

channels for better contacts with reactants. Kim et al. reported that the mesoporous TiO$_2$ with well-defined spherical shape show excellent photocatalysis ability in the degradations of methylene blue and acetaldehyde [27]. Since the nanospherical structure of mesoporous TiO$_2$ could enhance sufficient contact with reactant, it provides high specific surface area for increased reactive sites.

Further structural characterization of M-TiO$_2$ and Au/M-TiO$_2$ were carried out using transmission electron microscopy (TEM). The TEM and HRTEM images shown in Fig. 3a confirmed the ordered mesoporous structure and anatase crystalline of M-TiO$_2$ nanospheres. As
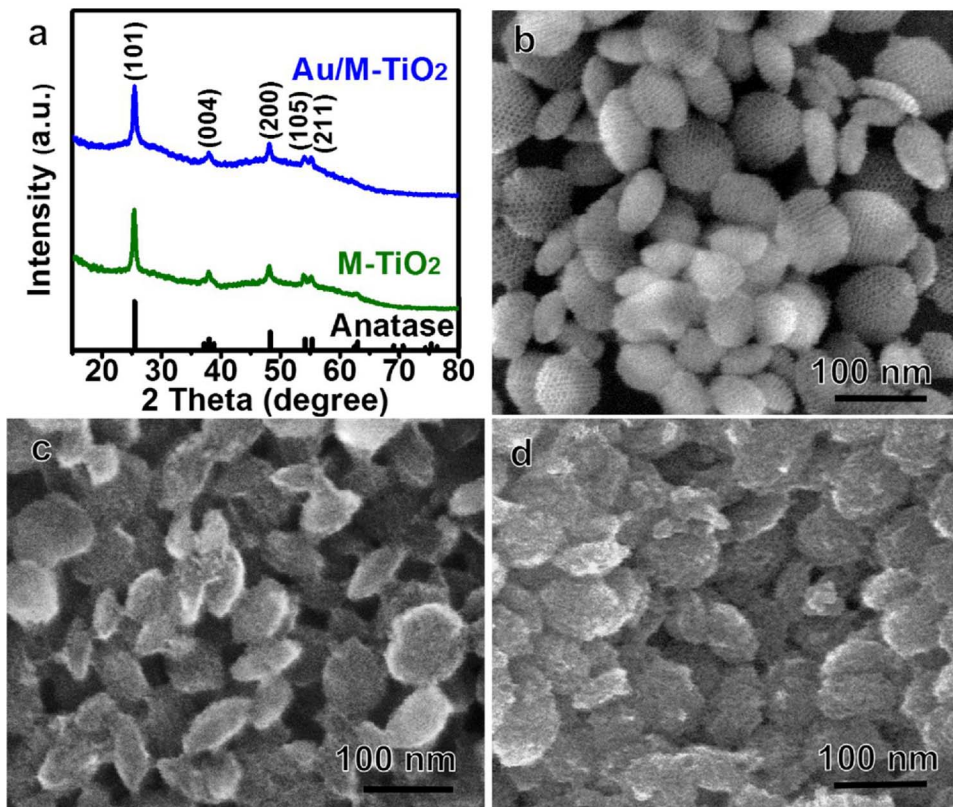

Fig. 2. (a) XRD patterns of M-TiO$_2$ and Au/M-TiO$_2$. The bottom pattern with vertical bars is derived from the JCPDS card (no. 21-1272) of tetragonal anatase. (b-d) SEM images of (b) MSN, (c) M-TiO$_2$ and (d)Au/M-TiO$_2$.
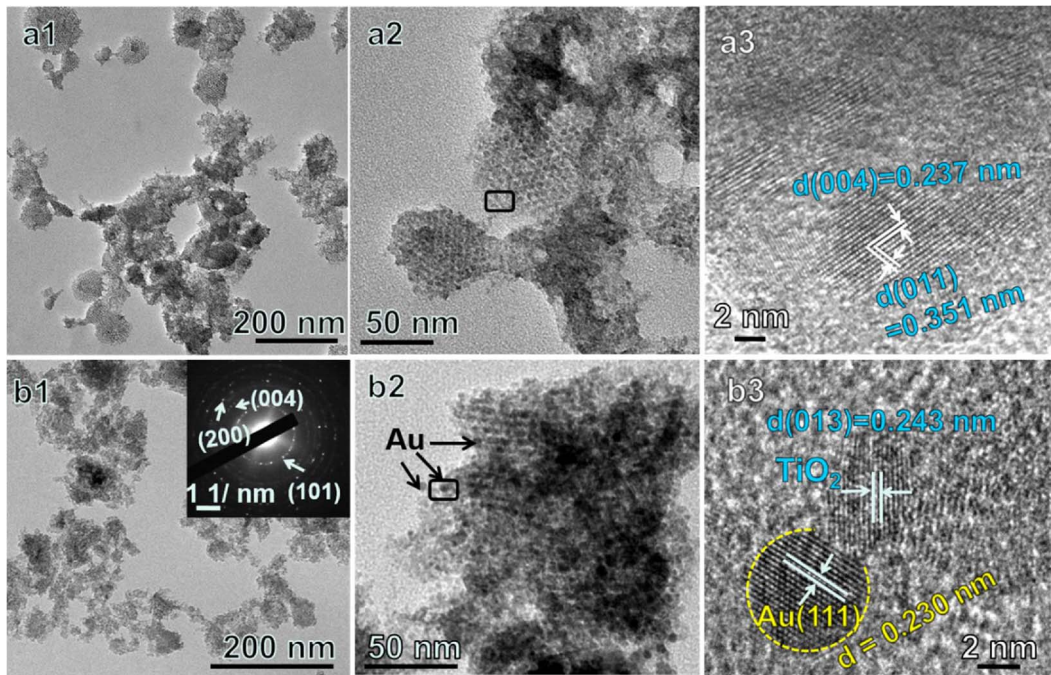
Fig. 3. (a1, a2) TEM images and (a3) high-magnification TEM images of M-TiO$_2$ from the area outlined by the rectangle in panel (a2). (b1, b2) TEM images and corresponding SAED pattern of Au/M-TiO$_2$, (b3) high-magnification TEM images of Au/M-TiO$_2$ from the area outlined by the rectangle in panel (b2).

shown in Fig. 3a2, the M-TiO$_2$ nanospheres were composed of oriented ultrasmall nanorods, and the diameter of each nanorods were ∼4 nm. The high-magnification micrographs in Fig. 3b1-2 demonstrate that the ordered mesoporous structure of M-TiO$_2$ was still preserved after loading Au NPs, and the Au NPs are highly dispersed on M-TiO$_2$ supports, the corresponding SAED pattern in Fig. 3b1 confirmed the anatase structure of M-TiO$_2$ in Au/M-TiO$_2$. Fig. 3b3 reveals that both Au NPs and M-TiO$_2$ are crystallized as evidenced from the well resolved Au (111) (d = 0.230 nm) and TiO$_2$ (013) (d = 0.243 nm) crystalline lattices. The precise element mappings in Fig. S1 reveals the Au NPs were uniformly dispersed in the mesoporous M-TiO$_2$. Furthermore, TEM analysis showed that the Au nanoparticles on the TiO$_2$ with a diameter of ∼ 3.15 nm (Fig. S2).

To investigate the localized surface plasmon resonance (LSPR) effect of Au/M-TiO$_2$, its light absorption properties were examined [28]. As seen in Fig. 4a, UV–vis spectra show broad absorption peaks for Au loaded M-TiO$_2$ at ∼530 nm, confirming the successful reduction of the Au precursor to the plasmonic Au NPs in the M-TiO$_2$. Pristine M-TiO$_2$ exhibits no absorption in the visible region, as expected. Meanwhile, we investigated the valence state of the deposited gold in Au/M-TiO$_2$ by X-ray photoelectron spectroscopy (XPS) (Fig. 4b). The XPS peaks observed at 83.3 and 87.0 eV are ascribed to metallic gold. The presence of Ti and O elements were also checked using XPS spectra in Fig. S3 corresponding to the Ti^{4+} and O^{2-} component in Au/M-TiO$_2$ [17]. The chemical compositions of the Au/M-TiO$_2$ were further examined by using energy dispersive X-ray (EDX) and inductively coupled plasma mass spectrometry ((ICP-MS)). A small amount of Si was observed in the Au/M-TiO$_2$ sample (Fig. S4) with an average atomic ratio of Si:Ti = 0.06, indicating that residual silica is possibly responsible for the formation of Si−O−Ti bonds in the TiO$_2$ crystals, and act as a bridge for the ordered mesoporous framework of Au/M-TiO$_2$ [26,29,30] after most of the silica were removed. Zhu et al. reported that these Ti−O−Si functional groups may even enhance the photocatalysis efficiency [6]. The small amount of residual Si may not only act as an interchannel bridge for the ordered mesorporous structure, but also promote the photocatalysis efficiency. Meanwhile, the (ICP-MS) result indicate the Au loading amount in Au/M-TiO$_2$ is 0.53 wt%.

Nitrogen adsorption-desorption isotherms were used to characterize
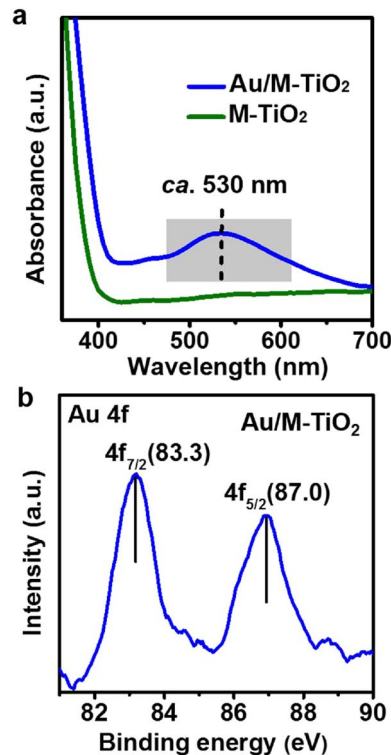
Fig. 4. (a) UV–vis absorption spectra of Au/M-TiO$_2$ and pristine M-TiO$_2$. (b) XPS spectra of Au element in Au/M-TiO$_2$.

the pore structure of samples. The nitrogen adsorption–desorption isotherms and corresponding pore size distribution plots of MSN, M-TiO$_2$ and Au/M-TiO$_2$ are shown in Fig. S5a and Fig. 5. The isotherms of both MSN (Fig. S5a), M-TiO$_2$ and Au/M-TiO$_2$ specimens show type IV curves with a hysteresis loop, indicating a mesoporous structure. The specific surface area, pore size, and pore volume of these porous materials are displayed in Table 1. The S_{BET} surface area of MSN is 870 m²/
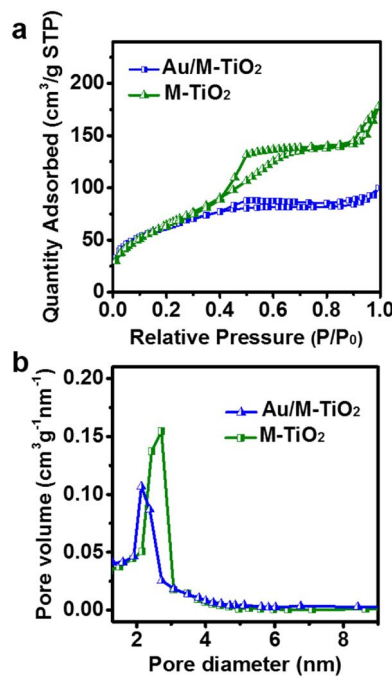
Fig. 5. (a) Nitrogen adsorption/desorption isotherms and (b) pore size distribution plots of M-TiO$_2$ and Au/M-TiO$_2$.

Table 1
Data of BET measurements of MSN, M-TiO$_2$ and Au/M-TiO$_2$.

Sample	Surface Area (m^2/g)	Pore Size (nm)	Pore Volume (cm^3/g)
MSN	870	3.9	0.84
M-TiO2	246	2.6	0.20
Au/M-TiO2	222	2.1	0.14

g, with a pore volume of 0.84 cm^3/g and pore size of 3.9 nm. Generally, the reported S_{BET} surface area of TiO$_2$ nanopowder is less than 100 m^2/g [22,23]. However, in our case, the surface area of M-TiO$_2$ is much higher (246 m^2/g) with a pore size of 2.6 nm. The pore geometry in the M-TiO$_2$ appears to be the same as the silica wall in MSN as they have a negative replication relationship. Meanwhile, the M-TiO$_2$ appeared to be arrays of nanorods with size ∼ 4 nm and the mesopore channel is ∼ 2.6 nm (Fig. 3a), consistent with the pore structure of the original MSN template. Subsequently, we modified M-TiO$_2$ with 3-aminopropyl-trimethoxysilane (APTES) for capture Au particles. As shown in Fig. S5b, the S_{BET} surface area of M-TiO$_2$-APTES is 236 m^2/g, which is not significantly decreased compared with bare M-TiO$_2$ (S_{BET} = 246 m^2/g). After loading Au nanoparticles, the S_{BET} surface area, pore size, and pore volume obviously decreased to S_{BET} = 222 m^2/g, pore size of 2.1 nm, and pore volume of 0.14 cm^3/g (Au/M-TiO$_2$), respectively. Thus, we deduce that (a) surface functionlization of APTES is rather limited to allow for catalytic action on TiO$_2$, (b) the Au nanoparticles are embedded into the mesopore nanochannels of M-TiO$_2$. The results confirmed the high surface area and mesoporous structure of Au/M-TiO$_2$. Additionally, the mesoporous structure of Au/M-TiO$_2$ can not only provide high specific surface area for increased reactive sites, but also offer confinement of Au nanoparticles in nanochannels for increased concentration and intimate contacts of reactants, which is most desirable for the applications in photocatalysis [31,32].

3.2. Photocatalytic performance

Recently, the development of "green" catalytic processes has gained increasing attention [7,10]. However, the use of hazardous solvents in organic chemical manufacturing creates undesirable environmental

Table 2
The photocatalytic oxidation of benzylamine into N-benzylidene benzylamine over various samples under visible-light irradiation.[a]

entry	catalyst	sel.(%)	conv. (%)	yield (mmol)	TOF (h^{-1})[b]	Au mass (wt%)
1	Au/M-TiO$_2$	99	12.5	1.73	178.6	0.53
2	Au/M-TiO$_2$[c]	99	9.0	1.30	134.2	0.53
3	Au/M-TiO$_2$[d]	–	–	–	–	0.53
4	Au/P25	98	8.1	1.16	113.3	0.56
5	Au/Acros anatase	80	9.2	1.05	100.8	0.57
6	M-TiO$_2$	99	3.3	0.47	–	–
7	Blank[e]	–	–	–	–	–
8	Au/rutile TiO$_2$[f] [13]	99	4.5	1.06	62.2	0.56

[a] Reaction conditions unless noted otherwise: 3 ml of benzylamine, 30 mg of catalyst, O$_2$ 1 atm, visible-light irradiation (λ > 420 nm) for 24 h, determined by GC using decane as an internal standard.
[b] TOF = the molecule number of the reacted benzylamine which turn into N-benzilidene benzylamine per hour/the number of Au atom.
[c] In air.
[d] In the absence of light.
[e] In the absence of catalyst.
[f] Ref. [13], 5.0 g of benzylamine, 50 mg of catalyst, in air, visible-light irradiation for 24 h.

footprints [8,33]. Sheldon et al. emphasized that "The best solvent is no solvent" [33]. Thus, in the drive towards achieving green catalysis, we investigated a solvent-free strategy for plasmonic photocatalysis of benzylamine to N-benzylidene benzylamine under visible light irradiation (λ > 420 nm). For comparison, the photocatalysis performance of bare M-TiO$_2$ and Au NPs loaded on Acros anatase and on Degussa P25 were studied under the same conditions. The results are shown in Table 2, the reaction neither proceeded without photocatalyst (Table 2, entry 7), nor without visible light irradiation (Table 2, entry 3), which confirms that the photocatalysis oxidation of benzylamine is a light-driven reaction. With 1 atm of O$_2$ as the oxidant, the photocatalyst Au/M-TiO$_2$ exhibited very high selectivity (99%) and a high yield (1.73 mmol, TOF = 178.6 h^{-1}) for the oxidation of benzylamine to N-benzylidene benzylamine. The yield with Au/M-TiO$_2$ is 1.5 and 1.6 times higher than that with Au/P25 (1.16 mmol, TOF = 113.3 h^{-1}) and Au/Acroc anatase (1.05 mmol, TOF = 100.8 h^{-1}) under the same conditions, respectively. More importantly, such a high yield is much better than most of the reported results on photocatalysis benzylamine oxidation as summarized in Table S1 [1,3,6,13–15,34–37]. Zhao and co-workers have reported that TiO$_2$ can photocatalyze amines to imines under visible light irradiation via a surface complex mechanism [1,32]. However, in our solvent-free system, the activity of Au/M-TiO$_2$ is much greater than that of bare M-TiO$_2$ (yield = 0.47 mmol, in Table 2, entry 6) under the same conditions, confirming the main role of plasmonic photocatalysis in Au/M-TiO$_2$ system [1,3,6,14,15,32–35]. Futhermore, we investigated the oxidation of benzylamine to N-benzylidene benzylamine in air atmosphere. As shown in entry 2, without adding dioxygen, the yield of N-benzylidene benzylamine can still reach 1.30 mmol with a TOF = 134.2 h^{-1}, which is two times higher than that of previously reported works of Tada et al (yield = 1.06 mmol, TOF = 62.2 h^{-1}, in Table 2, entry 8) with Au/rutile TiO$_2$ in a solvent-free system [13]. This result is also comparable with most of the reported works on photocatalysis benzylamine under O$_2$ atmosphere (Table S1) [1,3,32–35]. Meanwhile, the photocatalytsis reaction of amines to imines in acetonitrile as the solvent also follows the same tendency as in the solvent-free state (Table S2). The mesoporous Au/M-

Table 3
Aerobic oxidation of various amines to corresponding imines using Au/M-TiO$_2$.

entry	substrate	product	sel. (%)	conv. (%)	yield (mmol)
1			99	12.5	1.73
2			99	9.5	1.13
3			99	10.9	1.25
4			99	4.3	0.64

Reaction conditions: 3 ml of benzylamine, 30 mg of catalyst, O$_2$ 1 atm, visible-light irradiation (λ > 420 nm) for 24 h, determined by GC using decane as an internal standard.

TiO$_2$ photocatalysts exhibited very high selectivity (99%) and conversion (96%) for the oxidation of benzylamine to the corresponding imine in acetonitrile solvent within 8 h. These results indicate that the mesoporous Au/M-TiO$_2$ show much enhanced photocatalysis ability under visible light irradiation. The high efficiency may be attributed to two factors in the mesoporous structure: (a) more active sites and accessible molecular diffusion passway for active oxidation, (b) the confinement effect of the ordered nanopores in mesoporous Au/M-TiO$_2$ making the bi-molecular reaction highly preferred for promoting the selectivity in the plasmonic photocatalysis.

Additionally, the phtocatalytic activity of Au/M-TiO$_2$ was also examined for the oxidations of other benzylic amines to imines (Table 3). Relative high yields and selectivity (99%) were also observed within 24 h in the oxidations of amines to the corresponding imines. In general, electron-rich benzylamines (OMe and Me derivatives) could be oxidized faster than electron-deficient ones (Cl derivative) [32]. These results suggest that Au/M-TiO$_2$ are promising plasmonic photosensitizers for the oxidative coupling reactions of various amines [29,30].

Stability is also an important issue for an efficient photocatalyst. Therefore, the cycling performance of Au/M-TiO$_2$ for the oxidation of benzylamine to N-benzylidene benzylamine was evaluated under visible light irradiation (Fig. S6). The Au/M-TiO$_2$ exhibited good recyclability and slight difference in both relative activity (yield 1.73–1.50 mmol) and selectivity (99–96%) after 3 cycles. The results indicate good reusability and stability of Au/M-TiO$_2$.

3.3. Investigation of photocatalytic mechanism

Previous works on benzylamine photocatalysis gave two different reaction pathway [1,3,34]. Kim and Wang et al. proposed that the formation of imine involves a oxidative-dehydrogenation step and a further condensation step. The oxidative-dehydrogenation process occurrs first, with the formation of the intermediate imine (X−Ph−CH=NH) and H$_2$O$_2$ by the oxidation reaction of photogenerated superoxide radical (·O$_2^-$) and hole (h$^+$). Subsequently, the X−Ph−CH=NH condense with the residual amine to produce the desired imine products [34,36]. Meanwhile, another reaction mechanism proposed by Zhao et al. suggested that the selective oxygenation step ocurrs first, with the formation of the intermediate aldehyde, and then further condense into imine products (Fig. S7). [1,15].

Therefore, to elucidate the exact reaction mechnaism responsible for the oxidative coupling reactions of amines in our Au/M-TiO$_2$ system, further experiments were carried out to investigate the intermediate products during the photocatalysis reaction. However, since

the benzaldimine (X−Ph−CH=NH) and aldehyde intermediates are very reactive in the photocatalysis reaction of amine, these generated intermediates would soon condense with abundant amine in the solvent-free system, rendering the direct detection of intermediates practically impossible [3].

Firstly, we identified the active radical species involved in the photocatalytic process by the electron spin resonance (ESR) spectra spin-trap technique with 5,5-dimethyl-1-pyrroline N-oxide (DMPO) as the spin trapping compound (Fig. 6). The obviously characteristic peaks of DMPO-·O$_2^-$ were observed for Au/M-TiO$_2$, Au/P25 and Au/Acros anatase under visible light irradiation, confirming the generation of ·O$_2^-$ radicals [38]. Interestingly, the results demonstrate Au/M-TiO$_2$ can generate more ·O$_2^-$ radicals than Au/P25 and Au/Acros under visible light irradiation. It has been reported that the solubility of nonpolar gases such as N$_2$, CH$_4$ and CO$_2$ in liquid confined in nanoporous solid can be much higher than expected from the bulk solubility due to the oversolubility phenomenon. [38] The stronger solvent–solid interactions create regions of low solvent density in the confined solvent, enhancing gas uptakes [39–45]. Therefore, we expect the stronger ·O$_2^-$ signals can be attributed to the mesopores of Au/M-TiO$_2$ accommodating large quantities of dissolved O$_2$ in the nanopores of the host thus can produce more ·O$_2^-$ radicals to drive the photocatalysis [45].

Furthermore, we identified the production of H$_2$O$_2$ in the benzylamine coupling reaction mixture during the reaction by iodimetry
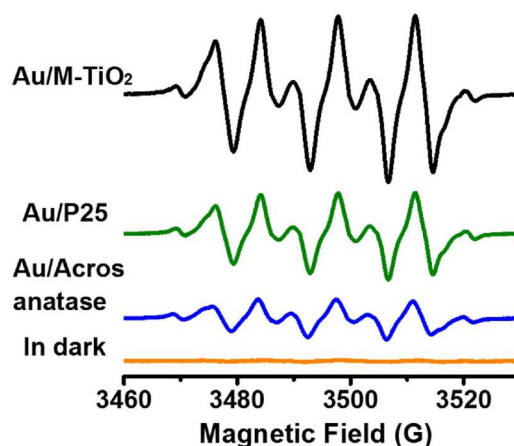

Fig. 6. DMPO spin-trapping ESR spectra of Au/M-TiO$_2$, Au/P25 and Au/Acros anatase in methanol dispersion for DMPO - ·O$_2^-$ under visible light irradiation and Au/M-TiO$_2$ in the absense of light, respectively.

Table 4
Aerobic oxidation of secondary benzylic amines by Au/M-TiO$_2$ under visible-light irradiation.

entry	substrate	conv. (%)	products (sel. %)
1		80	9 90
2		72	19 80
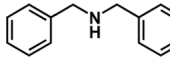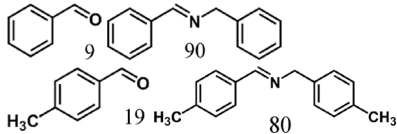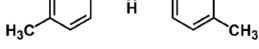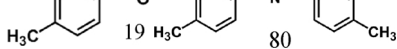
Reaction conditions: 0.2 mmol of amine, 20 mg of catalyst, 5 mL of CH$_3$CN, O$_2$ 1 atm, visible-light irradiation (λ > 420 nm) for 8 h, determined by GC using decane as an internal standard.

experiment and take starch as indicator [46]. As shown in Fig. S8, the color of the reaction solution become dark brown, while the neat benzylamine solution did not change colors, indicating the formation of iodine (I$_2$) in the reaction solution, which confirmed that H$_2$O$_2$ exists in the reaction mixture [46]. These results confirmed the existence of a oxidative-dehydrogenation process in our system. Subsequently, photocatalysis oxidation of secondary benzylic amines were performed to clarify the existence of oxygenation pathway (Fig. S7). If the reaction only operates along the oxidative-dehydrogenation pathway, the formation of imines from secondary benzylic amines should directly be oxidized to the corresponding imine according to Eq. 1. However, if the oxidative-dehydrogenation step and oxygenation step are coexistent in our system, the corresponding aldehydes (the oxygenation products) should be observed for the oxidation of these substrates (Eq. (2)) [3]. The results of photocatalysis oxidation of secondary benzylic amines are summarized in Table 4. Notably, a slight amount of the corresponding aldehydes were observed in the oxidation of both dibenzylamine and 4,4′-dimethyldiphenylamine, indicating the oxygenation step (Fig. S7) is a secondary pathway in the Au/M-TiO$_2$ system.

Moreover, since the plasmonic adsorption peak of Au/M-TiO$_2$ range from 480 to 600 nm with center at ∼530 nm, we further checked the role of plasmonic photocatalysis reaction of benzylamine to *N*-benzylidene benzylamine in Au/M-TiO$_2$ system under a different visible-light irradiation (λ > 495 nm). As shown in Table S3, the yield of *N*-benzylidene benzylamine is 1.32 mmol with a TOF = 135.7 h^{-1}, as the corresponding yield and TON are 1.73 and 178.6 under λ > 420 nm. This trend is consistent with the variation of absorption of a gold plasmonic absorption band. Meanwhile, the bare M-TiO$_2$ can achieve 0.47 mmol yield of *N*-benzylidene benzylamine (Table 2, entry 6), which is only a quarter of the yield by Au/M-TiO$_2$ (1.73 mmol, in Table 2, entry 1)."

Therefore, these results demonstrate that the oxidative-dehydrogenation process is the main reaction pathway in the Au/M-TiO$_2$ system while a fraction of the oxygenation step are processed simultaneously during the reaction. The two-pathway reactions coexist in Au/M-TiO$_2$ system, which contributes to the superior photocatalytic performance on oxidative coupling reactions of amines.

$$Ph\diagup NH \diagdown Ph \xrightarrow[\text{catalyst}]{vis} Ph \diagup N \diagdown Ph \qquad (1)$$

$$Ph\diagup NH \diagdown Ph \xrightarrow[\text{catalyst}]{vis} Ph \diagup O + Ph \diagup NH_2 \longrightarrow Ph \diagup N \diagdown Ph \qquad (2)$$
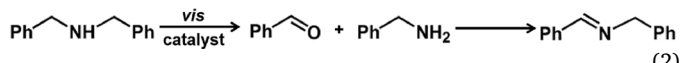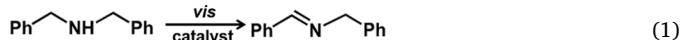
Consequently, the reaction mechanisms can be rationalized as shown in Fig. 7. Significantly, in pathway 1, the plasmon generated hot electrons transfer from the Au NPs to the M-TiO$_2$ supports under visible light irradiation and the reductive electrons on M-TiO$_2$ activate the adsorbed O$_2$ molecules into the reactive ·O$_2^-$ radicals (Fig. 7b) while the plasmonic holes left behind in the Au NPs–TiO$_2$ interface can abstract an electron from the benzylamine to yield a benzylamine radical cation [21]. Subsequently, the ·O$_2^-$ species would oxidate amines into benzaldimines (Ph−CH=NH) and H$_2$O$_2$. The H$_2$O$_2$ can also catalyze benzylamine into Ph−CH=NH, and the generated Ph−CH=NH further condenses with redundant amines into the corresponding imines [19].

Accordingly, this oxidative-dehydrogenation process is supposed to be induced by the plasmonic photocatalysis process of Au NPs loaded on M-TiO$_2$ [36]. Meanwhile, minor fraction of the reaction is processed through the photosensitization catalysis reaction by TiO$_2$-amide surface complex, which is mainly conducted on the TiO$_2$ support (Fig. S7) [11]. Therefore, the catalytic performances of these two pathways both depend critically on the mesoporous nature of the TiO$_2$ supports. The superior photocatalytic activity of mesoporous Au/M-TiO$_2$ can be attributed to the following reasons: (i) the confinement effect of the nanopores in mesoporous Au/M-TiO$_2$ can uptake more dioxygen, thus further promoted the formation of ·O$_2^-$ radicals (Fig. 6) and make the bi-molecular reaction highly preferred for promoting the selectivity and conversion in the plasmonic photocatalysis; (ii) the mesoporous Au/M-TiO$_2$ with a large specific surface area and pore volume can provide abundant sites and efficient contact area for dissociative adsorption of benzylamine molecules, further improving the plasmonic oxidation efficiency of benzylamine and enhancing the formation of TiO$_2$-amide surface complex for photosensitization; (iii) the plasmonic photocatalysis and TiO$_2$-amide photosensitization process simultaneously, thus enhancing the photocatalysis performance; (iv) the in-situ produced H$_2$O$_2$ promotes the oxidative coupling reactions to proceed more quickly. All these features make the Au/M-TiO$_2$ particularly attractive for applications in organic synthesis.

4. Conclusions

In summary, the ordered mesoporous Au/M-TiO$_2$ nanoparticles with anatase crystalline and a large specific surface area (222 m^2/g) has been successfully designed and synthesized by a facile hard-templating method. The mesoporous Au/M-TiO$_2$ with abundant interfacial area exhibited superior visible light photocatalytic performance in the selective oxidative coupling reactions of various amines in a green approach by utilizing dioxygen as an oxidant in a solvent-free environment at ambient temperature. The Au/M-TiO$_2$ can achieved higher yield than that of Au/P25 and Au/Acros anatase in the oxidation of benzylamine to *N*-benzylidene benzylamine. Importantly, high selectivity and outstanding yield of *N*-benzylidene benzylamine also can be achieved under air atmosphere in a solvent-free environment. The mechanism responsible for the Au/M-TiO$_2$-photocatalyzed oxidative coupling of the amines were fully investigated, which indicated the plasmonic photocatalysis act as a main reaction pathway, and photosensitization processes coexist during reactions. This report contributes to the use of visible light responsive TiO$_2$-based photocatalyst with high specific surface area to achieve green and high efficient organic synthesis.
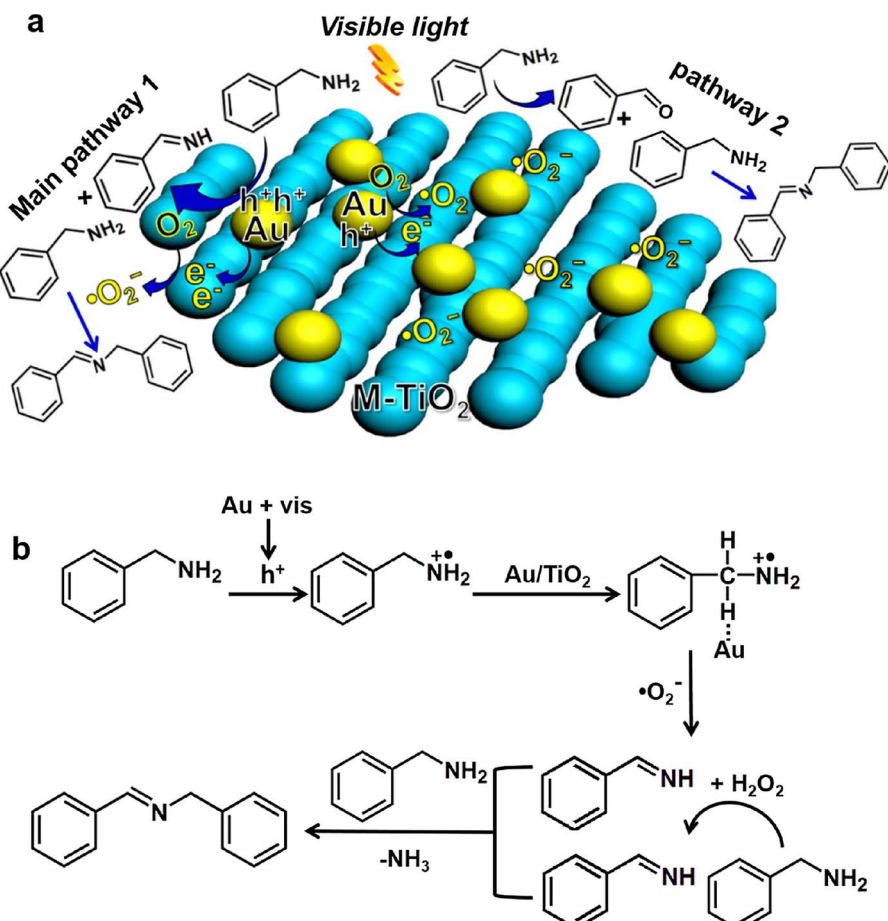
Fig. 7. (a) Scheme of the proposed mechanism and (b) main pathway for selective aerobic oxidation of benzylamine to N-benzylidene benzylamine over Au/M-TiO$_2$ under visible light irradiation.

Appendix A. Supplementary data

Supplementary material related to this article can be found, in the online version, at doi:https://doi.org/10.1016/j.apcatb.2018.02.054.

References

[1] X. Lang, H. Ji, C. Chen, W. Ma, J. Zhao, Selective formation of imines by aerobic photocatalytic oxidation of amines on TiO$_2$, Angew. Chem. Int. Ed. 50 (2011) 3934–3937.

[2] B. Yuan, R. Chong, B. Zhang, J. Li, Y. Liu, C. Li, Photocatalytic aerobic oxidation of amines to imines on BiVO$_4$ under visible light irradiation, Chem. Commun. 50 (2014) 15593–15596.

[3] S. Furukawa, Y. Ohno, T. Shishido, K. Teramura, T. Tanaka, Selective amine oxidation using Nb$_2$O$_5$ photocatalyst and O$_2$, ACS Catal. 1 (2011) 1150–1153.

[4] L. Aschwanden, T. Mallat, F. Krumeich, A. Baiker, A simple preparation of an efficient heterogeneous gold catalyst for aerobic amine oxidation, J. Mol. Catal. A: Chem. 309 (2009) 57–62.

[5] E. Guiu, B. Muñoz, S. Castillón, C. Claver, Iridium-catalyzed enantioselective hydrogenation of imines with xylose diphosphite and diphosphinite ligands, Adv. Synth. Catal. 345 (2003) 169–171.

[6] S. Zavahir, H. Zhu, Visible light induced green transformation of primary amines to imines using a silicate supported anatase photocatalyst, Molecules 20 (2015) 1941–1954.

[7] T. Wang, P. Zhang, Y. Sun, B. Liu, Y. Liu, Z.-A. Qiao, Q. Huo, S. Dai, New polymer colloidal and carbon nanospheres: stabilizing ultrasmall metal nanoparticles for solvent-free catalysis, Chem. Mat. 29 (2017) 4044–4051.

[8] R. Dhanda, M. Kidwai, Magnetically separable CuFe$_2$O$_4$/reduced graphene oxide nanocomposites: as a highly active catalyst for solvent free oxidative coupling of amines to imines, RSC Adv. 6 (2016) 53430–53437.

[9] K. Tanaka, F. Toda, Solvent-free organic synthesis, Chem. Rev. 100 (2000) 1025–1074.

[10] D.I. Enache, J.K. Edwards, P. Landon, B. Solsona-Espriu, A.F. Carley, A.A. Herzing, M. Watanabe, C.J. Kiely, D.W. Knight, G.J. Hutchings, Solvent-free oxidation of primary alcohols to aldehydes using Au-Pd/TiO$_2$ catalysts, Science 311 (2006) 362–365.

[11] X. Lang, J. Zhao, X. Chen, Visible-Light-Induced photoredox catalysis of dye-sensitized titanium dioxide: selective aerobic oxidation of organic sulfides, Angew. Chem. Int. Ed. 55 (2016) 4697–4700.

[12] X. Lang, X. Chen, J. Zhao, Heterogeneous visible light photocatalysis for selective organic transformations, Chem. Soc. Rev. 43 (2014) 473–486.

[13] S.-i. Naya, K. Kimura, H. Tada, One-step selective aerobic oxidation of amines to imines by gold nanoparticle-loaded rutile titanium (IV) oxide plasmon photocatalyst, ACS Catal. 3 (2012) 10–13.

[14] S. Furukawa, Y. Ohno, T. Shishido, K. Teramura, T. Tanaka, Reaction mechanism of selective photooxidation of amines over niobium oxide: visible-light-induced electron transfer between adsorbed amine and Nb$_2$O$_5$, J. Phys. Chem. C 17 (2012) 442–450.

[15] Y. Zhang, L. Pei, Z. Zheng, Y. Yuan, T. Xie, J. Yang, S. Chen, J. Wang, E.R. Waclawik, H. Zhu, Heterojunctions between amorphous and crystalline niobium oxide with enhanced photoactivity for selective aerobic oxidation of benzylamine to imine under visible light, J. Mater. Chem. A 3 (2015) 18045–18052.

[16] J. Schneider, M. Matsuoka, M. Takeuchi, J. Zhang, Y. Horiuchi, M. Anpo, D.W. Bahnemann, Understanding TiO$_2$ photocatalysis: mechanisms and materials, Chem. Rev. 114 (2014) 9919–9986.

[17] J. Yang, Q. Wu, S. He, J. Yan, J. Shi, J. Chen, M. Wu, X. Yang, Completely & 001& oriented anatase TiO$_2$ nanoarrays: topotactic growth and orientation-related efficient photocatalysis, Nanoscale 7 (2015) 13888–13897.

[18] X. Lang, W. Ma, C. Chen, H. Ji, J. Zhao, Selective aerobic oxidation mediated by TiO$_2$ photocatalysis, Acc. Chem. Res. 47 (2013) 355–363.

[19] X. Meng, L. Liu, S. Ouyang, H. Xu, D. Wang, N. Zhao, J. Ye, Nanometals for solar-to-chemical energy conversion: from semiconductor-based photocatalysis to plasmon-mediated photocatalysis and photo-thermocatalysis, Adv. Mater. 28 (2016) 6781–6803.

[20] L. Liu, X. Zhang, L. Yang, L. Ren, D. Wang, J. Ye, Metal nanoparticles induced photocatalysis, Natl. Sci. Rev. (2017) nwx019.

[21] S. Wang, Y. Gao, S. Miao, T. Liu, L. Mu, R. Li, F. Fan, C. Li, Positioning the water oxidation reaction sites in plasmonic photocatalysts, J. Am. Chem. Soc. 139 (2017)

11771–11778.

[22] W. Zhou, W. Li, J.-Q. Wang, Y. Qu, Y. Yang, Y. Xie, K. Zhang, L. Wang, H. Fu, D. Zhao, Ordered mesoporous black TiO$_2$ as highly efficient hydrogen evolution photocatalyst, J. Am. Chem. Soc. 136 (2014) 9280–9283.

[23] J. Yu, J. Low, W. Xiao, P. Zhou, M. Jaroniec, Enhanced photocatalytic CO$_2$-reduction activity of anatase TiO$_2$ by coexposed {001} and {101} facets, J. Am. Chem. Soc. 136 (2014) 8839–8842.

[24] Y.-W. Wang, K.-C. Kao, J.-K. Wang, C.-Y. Mou, Large-scale uniform two-dimensional hexagonal arrays of gold nanoparticles templated from mesoporous silica film for surface-enhanced Raman spectroscopy, J. Phys. Chem. C 120 (2016) 24382–24388.

[25] K.-C. Kao, C.-Y. Mou, Pore-expanded mesoporous silica nanoparticles with alkanes/ethanol as pore expanding agent, Micropor. Mesopor. Mater. 169 (2013) 7–15.

[26] W. Yue, C. Randorn, P.S. Attidekou, Z. Su, J.T. Irvine, W. Zhou, Syntheses, Li insertion, and photoactivity of mesoporous crystalline TiO$_2$, Adv. Funct. Mater. 19 (2009) 2826–2833.

[27] D.S. Kim, J.-D. Jeon, K.-H. Shin, The size-controlled synthesis of monodisperse spherical mesoporous TiO$_2$ particles and high dispersions of Pt, Pd, and Ag clusters on their surfaces, Micropor. Mesopor. Mater. 181 (2013) 61–67.

[28] Si. Naya, T. Niwa, R. Negishi, H. Kobayashi, H. Tada, Multi-Electron oxygen reduction by a hybrid visible-light-photocatalyst consisting of metal-oxide semiconductor and self-assembled biomimetic complex, Angew. Chem. Int. Ed. 53 (2014) 13894–13897.

[29] W. Yue, X. Xu, J.T. Irvine, P.S. Attidekou, C. Liu, H. He, D. Zhao, W. Zhou, Mesoporous monocrystalline TiO$_2$ and its solid-state electrochemical properties, Chem. Mat. 21 (2009) 2540–2546.

[30] B. Tian, X. Liu, H. Yang, S. Xie, C. Yu, B. Tu, D. Zhao, General synthesis of ordered crystallized metal oxide nanoarrays replicated by microwave-digested mesoporous silica, Adv. Mater. 15 (2003) 1370–1374.

[31] W. Dong, Y. Yao, L. Li, Y. Sun, W. Hua, G. Zhuang, D. Zhao, S. Yan, W. Song, Three-dimensional interconnected mesoporous anatase TiO$_2$ exhibiting unique photocatalytic performances, Appl. Catal. B: Environ. 217 (2017) 293–302.

[32] W. Dong, Y. Sun, W. Hua, Y. Yao, G. Zhuang, X. Lv, Q. Ma, D. Zhao, Preparation of secondary mesopores in mesoporous anatase–silica nanocomposites with unprecedented-high photocatalytic degradation performances, Adv. Funct. Mater. 26 (2016) 964–976.

[33] R.A. Sheldon, Green solvents for sustainable organic synthesis: state of the art, Green Chem. 7 (2005) 267–278.

[34] X. Lang, W. Ma, Y. Zhao, C. Chen, H. Ji, J. Zhao, Visible-Light-Induced selective photocatalytic aerobic oxidation of amines into imines on TiO$_2$, Chem. Eur. J. 18 (2012) 2624–2631.

[35] F. Raza, J.H. Park, H.-R. Lee, H.-I. Kim, S.-J. Jeon, J.-H. Kim, Visible-light-driven oxidative coupling reactions of amines by photoactive WS nanosheets, ACS Catal. 6 (2016) 2754–2759.

[36] Z. Yu, E.R. Waclawik, Z. Wang, X. Gu, Y. Yuan, Z. Zheng, Dual modification of TiNb$_2$O$_7$ with nitrogen dopants and oxygen vacancies for selective aerobic oxidation of benzylamine to imine under green light, J. Mater. Chem. A 5 (2017) 4607–4615.

[37] H. Chen, C. Liu, M. Wang, C. Zhang, N. Luo, Y. Wang, H. Abroshan, G. Li, F. Wang, Visible light gold nanocluster photocatalyst: selective aerobic oxidation of amines to imines, ACS Catal. 7 (2017) 3632–3638.

[38] Y. Shiraishi, S. Shiota, H. Hirakawa, S. Tanaka, S. Ichikawa, T. Hirai, Titanium dioxide/reduced graphene oxide hybrid photocatalysts for efficient and Selective partial oxidation of cyclohexane, ACS Catal. 7 (2016) 293–300.

[39] L.N. Ho, Y. Schuurman, D. Farrusseng, B. Coasne, Solubility of gases in water confined in nanoporous materials: ZSM-5, MCM-41, and MIL-100, J. Phys. Chem. C 119 (2015) 21547–21554.

[40] A. Luzar, D. Bratko, Gas solubility in hydrophobic confinement, J. Phys. Chem. B 109 (2005) 22545–22552.

[41] S. Miachon, V.V. Syakaev, A. Rakhmatullin, M. Pera-Titus, S. Caldarelli, J.A. Dalmon, Higher gas solubility in nanoliquids? ChemPhysChem 9 (2008) 78–82.

[42] V. Rakotovao, R. Ammar, S. Miachon, M. Pera-Titus, Influence of the mesoconfining solid on gas oversolubility in nanoliquids, Chem. Phys. Lett. 485 (2010) 299–303.

[43] N.L. Ho, J. Perez-Pellitero, F. Porcheron, R.J.-M. Pellenq, Enhanced CO$_2$ solubility in hybrid adsorbents: optimization of solid support and solvent properties for CO$_2$ capture, J. Phys. Chem. C 116 (2012) 3600–3607.

[44] E. Soubeyrand-Lenoir, C. Vagner, J.W. Yoon, P. Bazin, F. Ragon, Y.K. Hwang, C. Serre, J.-S. Chang, P.L. Llewellyn, How water fosters a remarkable 5-fold increase in low-pressure CO$_2$ uptake within mesoporous MIL-100 (Fe), J. Am. Chem. Soc. 134 (2012) 10174–10181.

[45] C.-C. Liu, C.-Y. Mou, S.S.-F. Yu, S.I. Chan, Heterogeneous formulation of the tricopper complex for efficient catalytic conversion of methane into methanol at ambient temperature and pressure, Energy Environ. Sci. 9 (2016) 1361–1374.

[46] A. Georgi, F.-D. Kopinke, Interaction of adsorption and catalytic reactions in water decontamination processes: part I. Oxidation of organic contaminants with hydrogen peroxide catalyzed by activated carbon, Appl. Catal. B: Environ. 58 (2005) 9–18.